Nonmigrating Diurnal Tides in Mesospheric and Lower-Thermospheric Winds and Temperatures

ELSAYED R. TALAAT AND RUTH S. LIEBERMAN

Space Physics Research Laboratory, University of Michigan, Ann Arbor, Michigan

(Manuscript received 11 August 1997, in final form 24 November 1998)

ABSTRACT

This paper presents analyses of nonmigrating diurnal tide signatures in High Resolution Doppler Imager mesospheric and lower-thermospheric winds and temperatures. A global comparison of both winds and temperature reveals equatorial features corresponding to nonmigrating tides. Structures interpreted as zonal mean and eastward nonmigrating diurnal tides display consistency between horizontal winds and temperatures. The second symmetric mode is prominent in the zonal mean and wavenumber 1. The gravest antisymmetric mode and the gravest symmetric or Kelvin mode are the main features in zonal wavenumbers 2 and 3. The amplitudes of the tides generally increase with altitude and maximize within 90–110 km.

1. Introduction

Diurnal thermal tides are global-scale inertia–gravity waves that oscillate with a period of one day. Solar thermal tides can be thought of as migrating and nonmigrating. The migrating diurnal tide is an oscillation with zonal wavenumber 1 that travels westward with the sun. Nonmigrating diurnal tides include any oscillation that is not traveling with the sun; examples are wavenumbers other than 1 or eastward propagating modes. Nonmigrating tides are functions of universal time, with or without zonal variation. Further theoretical descriptions of solar thermal tides can be found in Chapman and Lindzen (1970).

The strongest forcing of migrating tides is due to solar radiation absorption by tropospheric water vapor and stratospheric ozone (Lindzen 1967). The migrating (or sun-synchronous tide) is generated when the heating constituent is zonally uniform. Longitudinal variations in these constituents due to land–sea differences, topography, or latent heat release of diurnal oscillating clouds excite nonmigrating tidal modes (Kato et al. 1982; Forbes and Groves 1987; Kato 1989; Tsuda and Kato 1989; Lindzen 1978; Hamilton 1981). Lieberman and Leovy (1995) investigated several forcing mechanisms in a classical model with Newtonian cooling that extended into the lower mesosphere. Boundary layer sensible heat contributed the most to the nonmigrating surface pressure tide, while in the middle atmosphere the largest response was due to solar absorption with a weaker signal from latent heating. Williams and Avery (1996) used a dissipative f-plane model to investigate nonmigrating tides forced by the latent heat associated with diurnal oscillations of deep convective clouds. The superposition of nonmigrating tides was found to be of comparable amplitude to the migrating tide in the mesosphere and lower-thermosphere (MLT) region. Hagan et al. (1997) expanded the study by using the latent heat release functions of Williams and Avery to force tidal oscillations in a two-dimensional, linearized, steady-state tidal model. The nonmigrating components were strong enough to modulate the migrating tide zonally. Ekanayake et al. (1997) forced nonmigrating tides in a two-dimensional model using tropospheric forcing obtained from a GCM and found that in the low-latitude zonal wind, eastward diurnal tides were preferentially propagated over westward nonmigrating tides due, in part, to filtering by the mean zonal wind.

Departures from migrating diurnal structure in observational studies have suggested the presence of nonmigrating tides. Wallace and Tadd (1974) analyzed 12-h differences in rawinsonde data and found higher-order zonal structure, which they believed was due mainly to nonmigrating tides. Khattatov et al. (1996) postulated that differences between High Resolution Doppler Imager (HRDI) and medium-frequency radar determination of tides could be explained by nonmigrating components of significant amplitude. Lieberman (1991) analyzed nonmigrating tides in the stratosphere and lower mesosphere using Limb Interferometer Monitor of the Stratosphere (LIMS) data. The most prominent mode

Corresponding author address: Elsayed R. Talaat, The Johns Hopkins University, Applied Physics Laboratory, 11100 John Hopkins Road, Laurel, MD 20723-6099.
E-mail: elsayed.talaat@jhuapl.edu

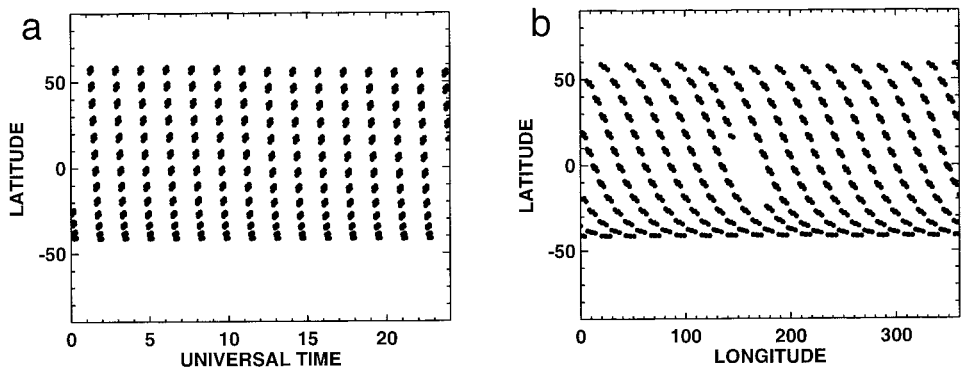

FIG. 1. HRDI daytime measurement locations for 15 Aug 1994 as a function of (a) Universal time and (b) longitude.

observed was the zonally symmetric diurnal tide, a standing wave uniform in longitude that oscillates with a period of one day. At low latitudes, the nonmigrating tides were observed to be vertically propagating. The features found in LIMS data exhibited some properties such as upward or no vertical phase propagation that could not be explained by a classical tidal model (Lieberman and Leovy 1995).

This study extends the global picture of nonmigrating tides into the equatorial MLT region using winds and temperatures measured by HRDI. A description of the data and the method of analysis used follow in section 2. Section 3 presents results from the analysis and section 4 includes a discussion and summary.

2. Data and analysis

This study uses horizontal wind and temperature measurements by HRDI on board the *Upper Atmosphere Research Satellite* (*UARS*). HRDI measures daytime winds and temperatures from 50 to 115 km and nighttime winds at 95 km. The longitudinal sampling is nominally 24°, and sampling along the orbital track is 500 km. Winds and temperatures are reported every 2.5 km in the vertical. HRDI (Hays et al. 1993) is a triple etalon Fabry–Perot interferometer, which infers mesospheric and lower-thermospheric winds from Doppler shifts in the O_2A band emission lines (Abreu et al. 1989). The precision of HRDI winds in the MLT region is roughly 5 m s^{-1} (Burrage et al. 1996b). Temperature and band volume emission rate (VER) are derived from the brightnesses of two rotational lines in the O_2A band (Ortland et al. 1998). A forward model is constructed to model brightness, and the difference between the initial computed brightnesses and those measured is inverted via perturbation theory to derive both temperature and VER. An individual profile is recovered with an error of 7 K.

UARS is in a slowly precessing orbit and samples roughly the same local time at every point along a latitude circle. A typical HRDI day of sampling, 15 August 1994, is presented in Fig. 1a. HRDI has full coverage of equatorial latitudes and samples 24 h of universal time. Figure 1b indicates the positions of each orbit as a function of latitude and longitude. From Figs. 1a and

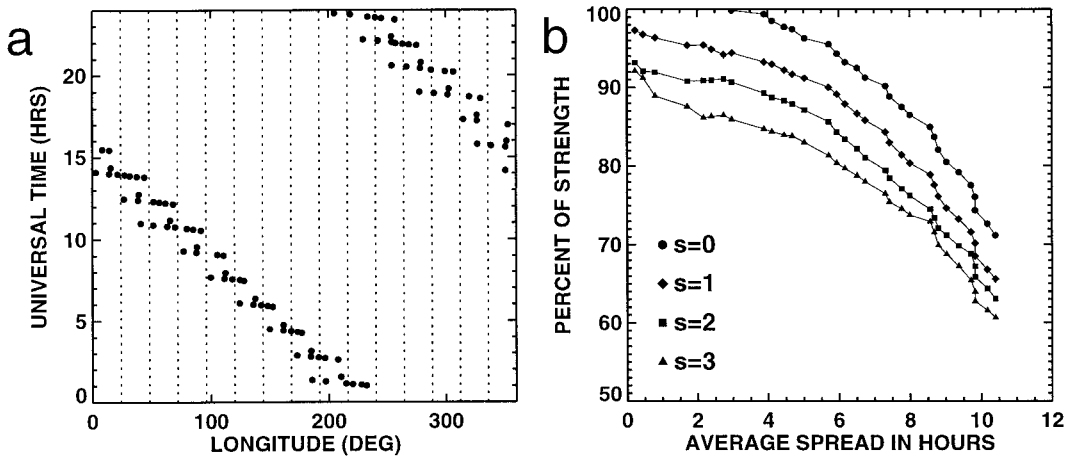

FIG. 2. (a) Dec 1992 data points at the equator plotted against longitude and Universal time. (b) Dilution of $s = 0$–3 eastward diurnal spectra due to the Universal time spread along the satellite coordinate, s_a.

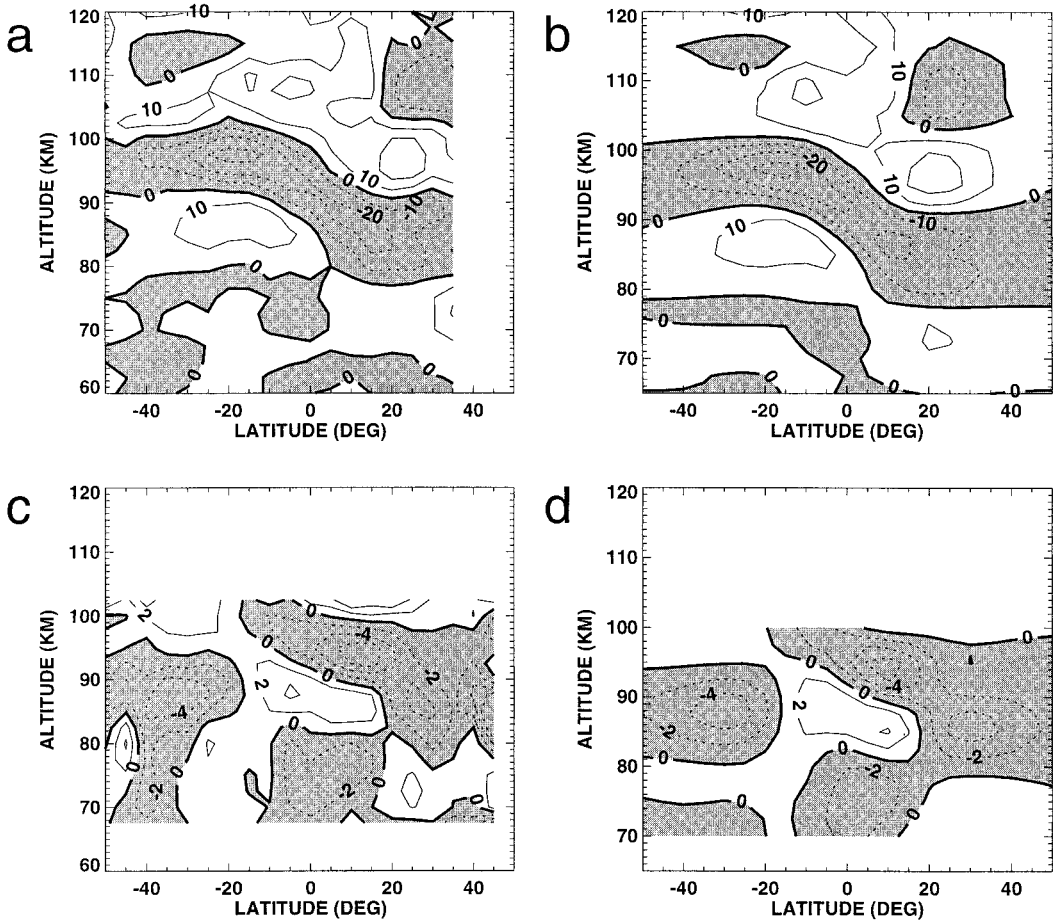

FIG. 3. Zonally symmetric diurnal tide at 0000 UTC for Nov 1994. (a) Raw meridional wind field, (b) meridional wind field projected onto the five lowest tidal functions, (c) raw temperature field, (d) temperature field projected onto the five lowest Hough functions. Winds are in meters per second and temperature in Kelvin.

1b, it can be seen that a complete latitude circle is sampled over 24 h of universal time.

The analysis of HRDI data requires several steps in order to retrieve a quantitative picture of diurnal nonmigrating tides. For a given day, the zonal mean wind and temperature are removed from each latitude and altitude. Because each point around a latitude circle is sampled at the same local time, by removing the zonal mean, the migrating tide is also removed (Morton et al. 1993; Hays et al. 1994; Lieberman and Riggin 1997). At each latitude and each altitude, data are then compiled to form monthly composites with respect to a satellite-relative (asynoptic) coordinate (Salby 1982) defined as

$$s_a = \frac{|c_0|\lambda - t}{\sqrt{1 + c_0^2}}, \tag{1}$$

where λ is longitude, t time, and c_0 the angular velocity of the satellite (≈ -6.37 rad day^{-1} day for *UARS*).

Figure 2a presents the composite at the equator for a representative month, December 1992. This composite is averaged within the grid lines shown to obtain the s_a coordinate. Within each bin, several hours of universal time are averaged together resulting in some dilution of the spectra. The loss of signal is quantified as a function of the time spread in Fig. 2b for different zonal wavenumber, s, eastward diurnal tides.

A Fourier harmonic in the satellite-relative coordinate, labeled k_{s_a}, is related to ground-based frequency, σ, and zonal wavenumber, s, by

$$k_{s_a} = \frac{|c_0|s - \sigma}{\sqrt{1 + c_0^2}}. \tag{2}$$

An observed peak in the satellite spectrum (k_{s_a}) can correspond to a number of wavenumber–frequency pairs, (s, σ), that are aliased to that particular k_{s_a} by the satellite motion relative to Earth (Salby 1982). For example, the zonally symmetric diurnal ($s = 0$, $\sigma = -2\pi$) is aliased to $k_{s_a} \approx 1$, as is a stationary ($\sigma = 0$) $s = 1$ zonal feature (k_{s_a}s are generally noninteger; but for discussion purposes, they will be referred to by their nearest integer value). Table 1, adapted from Lieberman

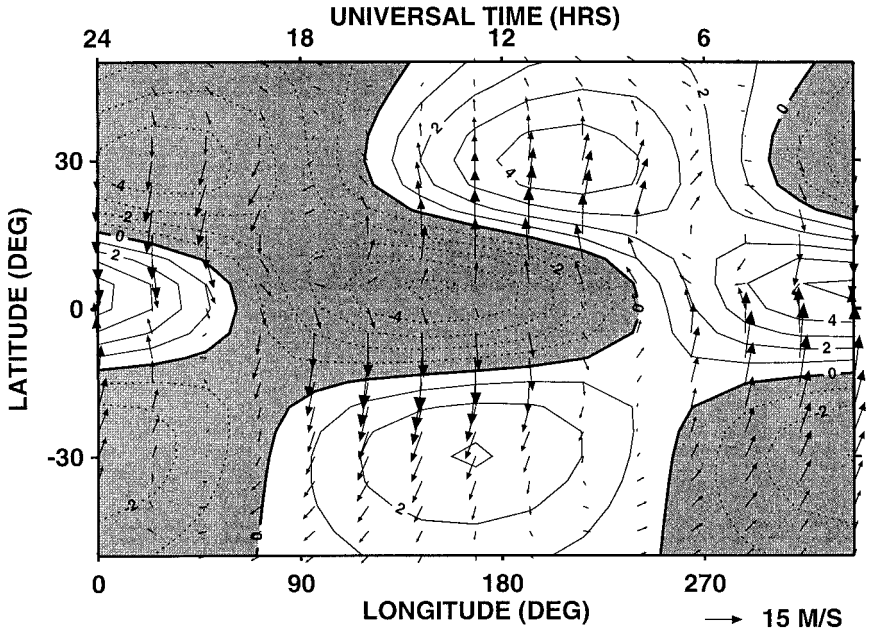

FIG. 4. Satellite $k_{s_a} = 1$ horizontal wind vector field at 85 km. Contours of temperature perturbation are overlaid. Contour levels are 1 K, with dotted lines indicating negative perturbation.

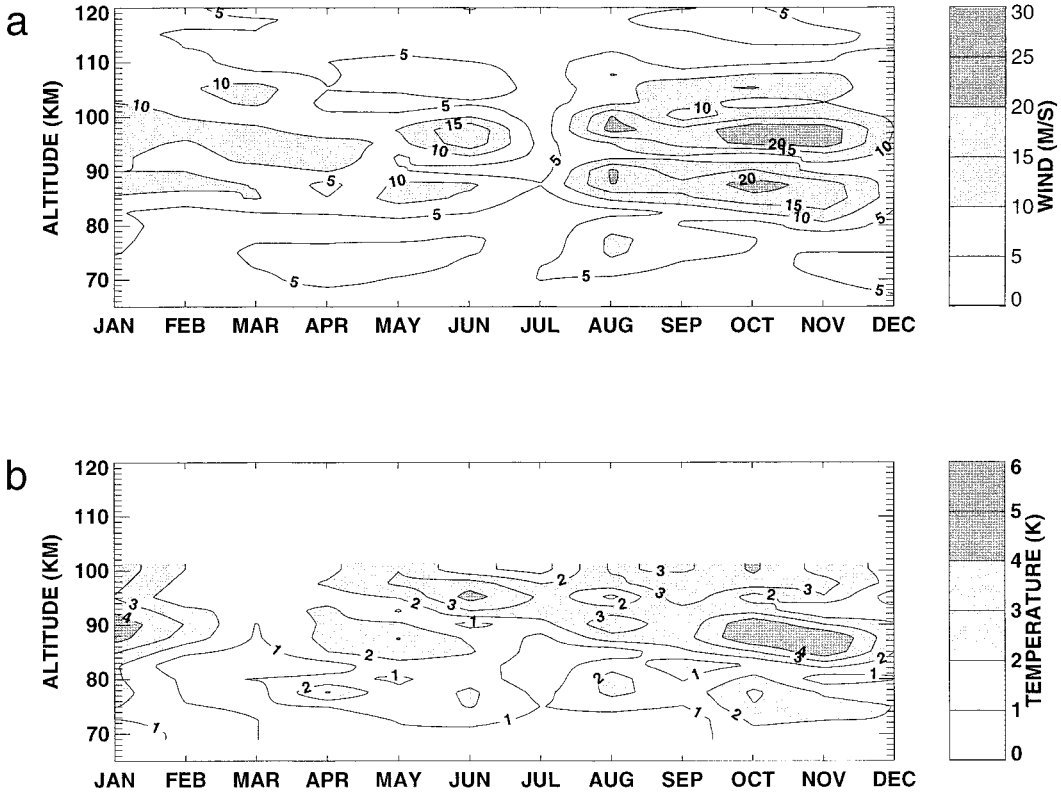

FIG. 5. Amplitude over time and altitude of the diurnal $s = 0$ second symmetric mode for (a) meridional wind (meters per second) and (b) temperature (Kelvin).

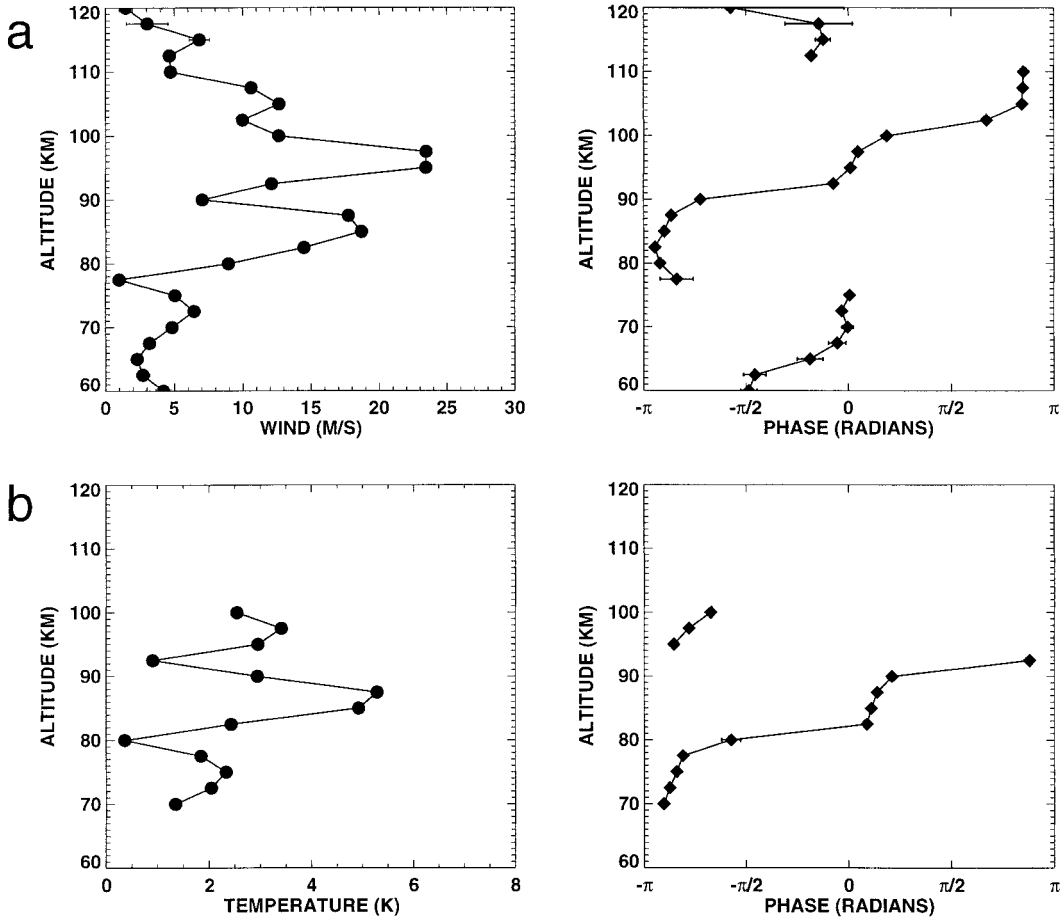

FIG. 6. Vertical structure of the amplitude and phase of the diurnal second symmetric $s = 0$ mode for Nov for (a) meridional wind, (b) temperature. Uncertainty estimates are determined through propagation of errors through the analysis.

(1991), presents the zonal wave components retrieved from HRDI data and some of their possible aliases. The $s = 0$ and eastward diurnal tides $s = 1$–3 are aliased to $k_{s_a} = 1$–4. Stationary $s = 1$–4 waves are observed at their true wavenumber. Westward $s = 2$–5 diurnal tides are also aliased to $k_{s_a} = 1$–4. Smaller-scale and faster waves are assumed to be averaged out by the composite.

Salby (1982) has shown that if data are sampled at two different local times (e.g., on the ascending and the descending nodes of the satellite orbit) it is possible to separate the contribution of two waves in the absence of the third. In general, HRDI samples at one local time per day for all altitude ranges; except at 95 km, where nighttime horizontal wind measurements are enabled. In theory, double-node separation of the winds is then possible at 95 km. However, the presence of a third wave would still alias into the retrieved spectra of the other two. In order to successfully resolve the contribution of three waves, sampling of data taken at three or more local times is required.

In the absence of a quantitative method of determining which wavenumber–frequency pair is present in the data, this decision is based upon comparison of the wind and temperature fields with theoretical features of the waves in question.

TABLE 1. Interpretation of observed satellite spectra. Top row: wavenumber observed by the satellite, in cycles per day. Remaining rows: the zonal wavenumber of the waves at the indicated frequency that are Doppler-shifted to the observed, satellite-relative wavenumber k_{s_a} (Salby 1982).

Satellite observed		$k_{s_a} = 0\ 1\ 2\ 3\ 4$
Stationary	$\sigma = 0$	$s = 0\ 1\ 2\ 3\ 4$
Eastward diurnal	$\sigma = -2\pi$	$s = \ \ 0\ 1\ 2\ 3$
Westward diurnal	$\sigma = 2\pi$	$s = 1\ 2\ 3\ 4\ 5$

3. Results

Prominent equatorial structures are found in $k_{s_a} = 1$–4 winds and temperatures. Figure 3a displays an altitude–latitude cross section of $k_{s_a} = 1$ meridional wind field for November 1994 at 0000 UTC. In this representative plot, the meridional wind is antisymmetric

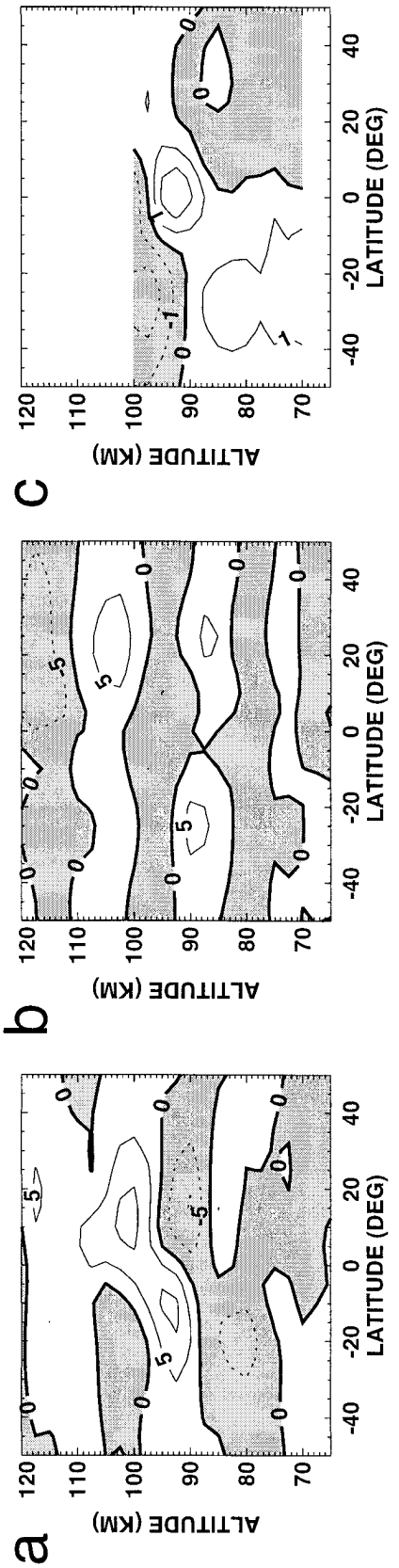

FIG. 7. Eastward $s = 1$ diurnal tide at 0000 UTC and 0° longitude for Sep for (a) meridional wind, (b) zonal wind, and (c) temperature.

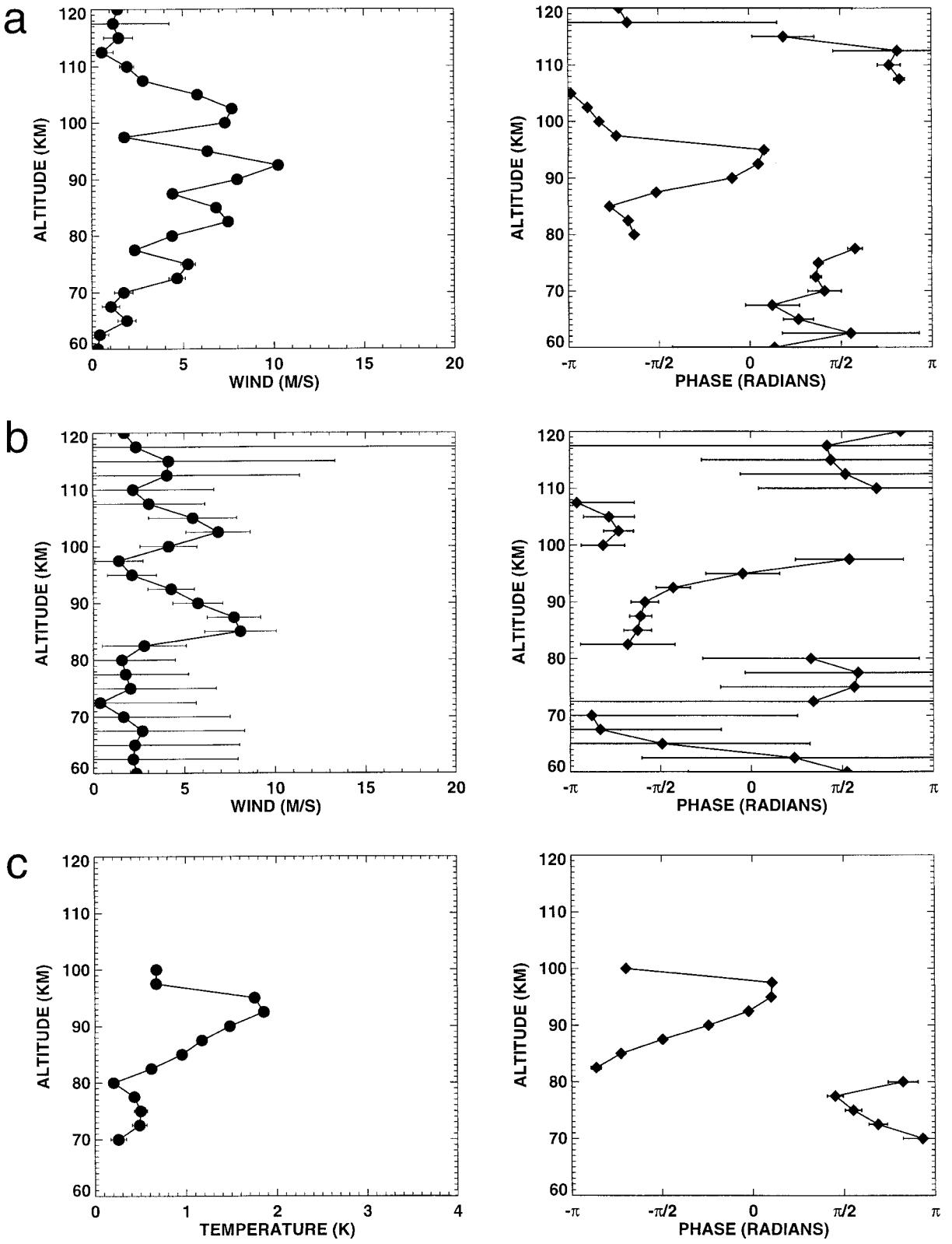

FIG. 8. Vertical structure of the amplitude and phase of the eastward diurnal $s = 1$ second symmetric mode for Sep for (a) meridional wind, (b) zonal wind, and (c) temperature.

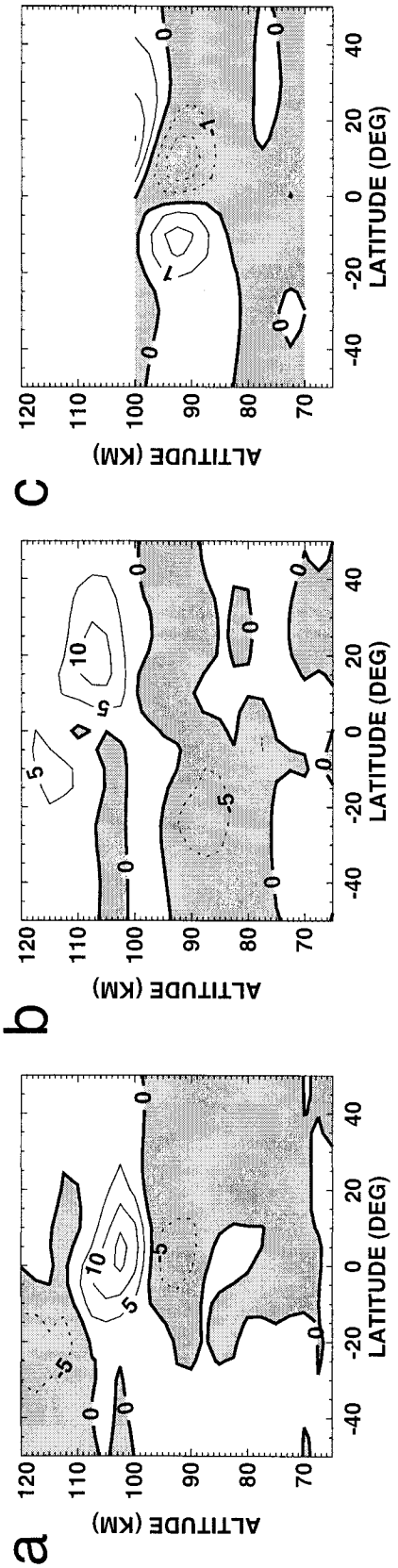

FIG. 9. Eastward $s = 2$ diurnal tide at 0000 UTC and 0° longitude for Aug for (a) meridional wind, (b) zonal wind, and (c) temperature.

about the equator, peaks at roughly 20°, and extends to about 40° on either side of the equator. This corresponds well to the theoretical meridional wind structures of the zonally symmetric diurnal tide. Figure 4 presents $k_{s_a} = 1$ wind vectors at 85 km overlaid with contours of temperature perturbation. This retrieval is plotted as a function of longitude and universal time. The convergence and divergence of the horizontal wind at the equator and the corresponding temperature perturbation are strong tidal characteristics. At low latitudes, $k_{s_a} = 1$–4 are believed to be predominantly tidal with correlating features in temperature and at least one horizontal wind component. In the following sections, these tidal features are referred to as *eastward tides,* as the observations generally suggest the presence of eastward over westward tides (section 4 has further discussion of this assumption).

Nonmigrating tides are observed in zonal and meridional winds and temperature from February 1992 to March 1995. Interannual variability can not be readily discerned from the dataset partly due to large gaps in the sampling; therefore, 3 yr of data are used to construct one composite year by averaging the spectra of individual months together. The results presented for diurnal $s = 0$–3 tides are those that exhibited organized and repeatable patterns in at least two out of the three fields observed.

a. Zonally symmetric diurnal tide

The dominant features displayed in the $k_{s_a} = 1$ field are interpreted as the zonally symmetric diurnal tide. August through November are the peak months for $s = 0$ tidal oscillations. During this period the meridional tidal wind is antisymmetric about the equator up to about 100 km, where the field becomes symmetric with maxima near or on the equator. During the same period of the year, the temperature field (Fig. 3c) is generally symmetric about the equator throughout the altitude range. Some antisymmetry causes the equatorial pattern to shift slightly off the equator. Above 90 km, antisymmetry is present away from the equator as well. The $s = 0$ zonal wind (not shown) exhibits features uncorrelated with those of the meridional and temperature fields, suggesting that quasi-stationary nontidal variability is heavily aliasing into the wind field (see Table 1).

Decomposing the measurement fields into separate tidal modes highlights similar properties between the fields. Meridional, zonal wind, and temperature tidal modes are denoted by V_n^s, U_n^s, and T_n^s, respectively, where s is the zonal wavenumber and n is the meridional index (Chapman and Lindzen 1970). Figures 3b and 3d display the November 1994 meridional wind and temperature fields, respectively, after orthogonal projection onto the lowest five vertically propagating tidal structures using singular value decomposition. This procedure smooths the field, while retaining all the salient features. For the meridional wind, the altitudes roughly below 100 km are well described by the second symmetric mode, V_2^0, and those above 100 km by a combination of V_2^0 and the gravest antisymmetric mode, V_1^0. Both $s = 0$ meridional wind and temperature show dominance of the second symmetric mode. The individual month tidal mode spectra are averaged to create one composite year. The amplitudes of V_2^0 and T_2^0 retrievals over altitude and time are presented in Fig. 5a and 5b, respectively. The amplitudes correspond to tidal modes normalized to a maximum value of one. The two fields correlate extremely well with peak amplitudes found during the same periods. The V_2^0 mode maximizes at 30 m s^{-1} in the 95–100-km region, while T_2^0 peaks at 6 K in a somewhat lower altitude range, 87–97 km.

Figure 6 shows the vertical structure of the amplitude and phase of V_2^0 and T_2^0 for the 3-yr averaged November. The V_2^0 mode increases with altitude, peaks at 95 km, and decreases at levels above. The T_2^0 mode also increases with altitude, maximizes at 87 km, and increases above 92 km. The phase of both fields generally increases with altitude and suggests that the vertical wavelength is 20–25 km in the region of 80–110 km (linear tidal theory predicts 24 km in an isothermal atmosphere of 200 K). Phase is defined as ϕ in the expression describing the evolution of a tide of zonal wavenumber, s, and eastward diurnal frequency, $\sigma = -2\pi$, as

$$A_s^\sigma \cos(s\lambda + \sigma t + \phi). \tag{3}$$

Below 80 km, the wavelength often appears to be longer. The temperature leads the meridional wind by roughly half a cycle, in accordance with linear tidal theory. The phase for the meridional wind is zero at roughly 95 km for periods around the equinox, while zero at near or above 100 km around the solstice.

b. Eastward s = 1 diurnal tide

The $k_{s_a} = 2$ field, interpreted as the $s = 1$ eastward diurnal tide, is strongest immediately following solstice periods. The meridional wind at 0000 UTC 0° longitude for a representative month, September, is presented in Fig. 7a. All three fields for this representative month display clear tidal structure that is variable in its symmetry. Antisymmetry about the equator is the dominant feature at lower altitudes, with symmetric structure prevailing above 95 km. The zonal wind (Fig. 7b) is generally symmetric, with maxima near 25°. Some hemispheric asymmetry in the structure becomes more pronounced at higher altitudes. Figure 7c reveals that the temperature is rich with both antisymmetric and symmetric structures about the equator. Below 90 km the field is generally antisymmetric, and above 90 km it becomes increasingly symmetric.

Tidal mode decomposition reveals that the second symmetric propagating mode displays good correlation between all three fields. This mode is present during most of the year, maximizing during April. The vertical

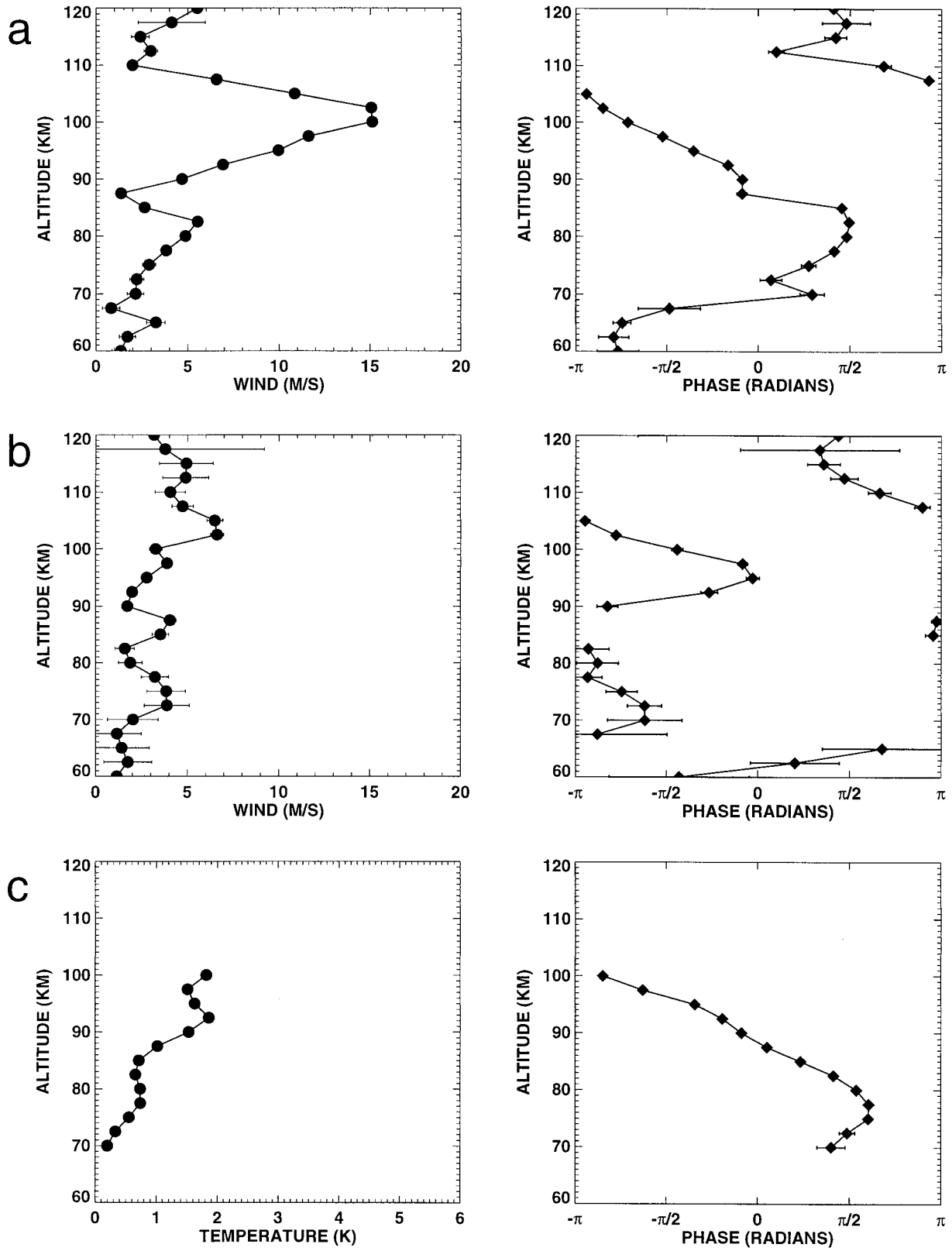

FIG. 10. Vertical structure of the amplitude and phase of the eastward diurnal $s = 2$ gravest antisymmetric mode for Aug for (a) meridional wind, (b) zonal wind, and (c) temperature.

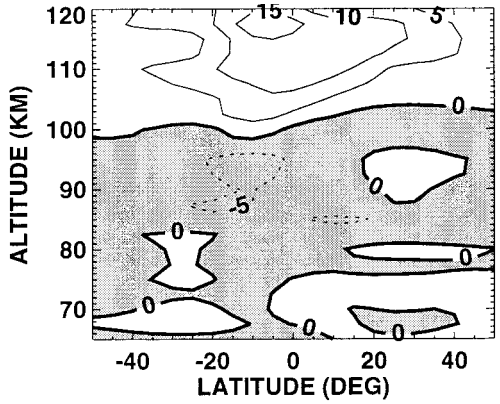

FIG. 11. Eastward $s = 2$ zonal wind diurnal tide at 0000 UTC for Dec.

structure of the amplitude and phase of the second symmetric mode for the representative month, September, is presented in Fig. 8. The V_3^1 mode peaks in amplitude at 92 km, U_3^1 at 85 km, and T_3^1 at 92 km. The zonal wind often maximizes at a higher altitude than the meridional wind and temperature. For this month, the phase is predominantly decreasing with altitude. The phase increases in altitude above 95 km for V_3^1 and T_3^1, and above 102 km for U_3^1. From month to month, the phase of this mode is variable, sometimes displaying increasing phase with height, as well as phase reversals in the middle of the altitude range.

c. Eastward $s = 2$ diurnal tide

The $k_{s_a} = 3$ field is believed to be dominated by the $s = 2$ eastward diurnal tide, which is present throughout the year. The meridional wind at 0000 UTC 0° longitude for the representative month of August is presented in Fig. 9a. The field maximizes near the equator and is mainly symmetric about the equator, with antisymmetry found at higher latitudes that is more prominent near equinox. Figure 9b presents the zonal wind field. The zonal wind generally has significant amplitude above 95 km, and in August it is both symmetric and antisymmetric about the equator. The August temperature (Fig. 9c) shows clear antisymmetric structure about the equator above 80 km.

The gravest antisymmetric mode can be correlated between all three fields. The V_3^2 mode typically maximizes around 15 m s^{-1}. The U_3^2 mode generally has lesser amplitude than V_3^2, and the locations of maxima are often at slightly higher altitudes: V_3^2 peaks between 97–105 km, while 100–107 km is the region of maximum U_3^2. The T_3^2 mode usually increases with altitude until 100 km. Figure 10 plots the amplitudes and phases for August. The phase of all three fields generally decreases with altitude and the observed wavelength is roughly 30 km (tidal theory predicts 34 km). Above 90 km, the winds and temperature are at roughly the same phase (tidal theory predicts that the phase of three fields are separated by roughly a quarter cycle).

Figure 11 presents the zonal wind during December. For this and other months near the solstice, symmetric structures with maxima centered near or on the equator dominate the zonal wind above 105 km. When these structures are interpreted as the gravest symmetric propagating tidal mode (diurnal Kelvin wave), they appear to have very long wavelengths at higher altitudes and amplitudes of 20 m s^{-1}.

d. Eastward $s = 3$ diurnal tide

The $k_{s_a} = 4$ field is interpreted as the $s = 3$ eastward diurnal tide. The $s = 3$ meridional wind primarily maximizes on or near the equator and is symmetric about the equator. Figure 12a presents a representative month, August, at 0000 UTC and 0° longitude. The symmetric equatorial meridional wind is present throughout the year except during May and June. The zonal wind (Fig. 12b) exhibits antisymmetry below 100 km and an equatorially centered structure with wide symmetric latitudinal extent above. This structure is dominant during the latter half of the year. During the rest of the year, the antisymmetric structure, seen below 100 km in Fig. 12b, extends into higher altitudes. The temperature field in Figure 12c has wide symmetric structure about the equator, with antisymmetry below 95 km.

The broad symmetry in both the temperature and zonal wind projects heavily on to the U_3^3 and T_3^3 modes, and is interpreted as the gravest symmetric propagating tidal mode, a diurnal Kelvin wave. Figure 13 presents the amplitudes of U_3^3 and T_3^3 over time. The U_3^3 mode peaks at 30 m s^{-1} and T_3^3 at 6 K. High amplitudes are generally located above 95 km during July–November. The consistency between T_3^3 and U_3^3 is very good; with amplitude peaks during the same periods and at approximately the same altitudes. Figure 14 displays the amplitude and phase structure of this mode for the representative month, August. The zonal wind amplitude peaks at 105 km (maxima generally lie between 102 and 110 km). The phase is decreasing with altitude, and the vertical wavelength is around 40 km (tidal theory predicts a wavelength of 52 km). The zonal wind leads the temperature by roughly a quarter cycle (tidal theory predicts a slightly larger lead).

As discussed in section 2 and Table 1, nonmigrating tides are aliased by stationary or slow planetary waves. Specifically, the gravest symmetric tidal or ''Kelvin'' modes of $s = 2$ and 3, could, in theory, correspond to low-frequency Kelvin waves. However, the observed vertical wavelengths of U_2^2 and U_3^3 agree well with those predicted for the diurnal tide, while those of a slow Kelvin wave are predicted to be much shorter. Furthermore, slow Kelvin waves would attenuate during periods of weakly eastward zonal mean winds. Observations show the eastward diurnal modes maximize during July–August, when the equatorial MLT zonal mean

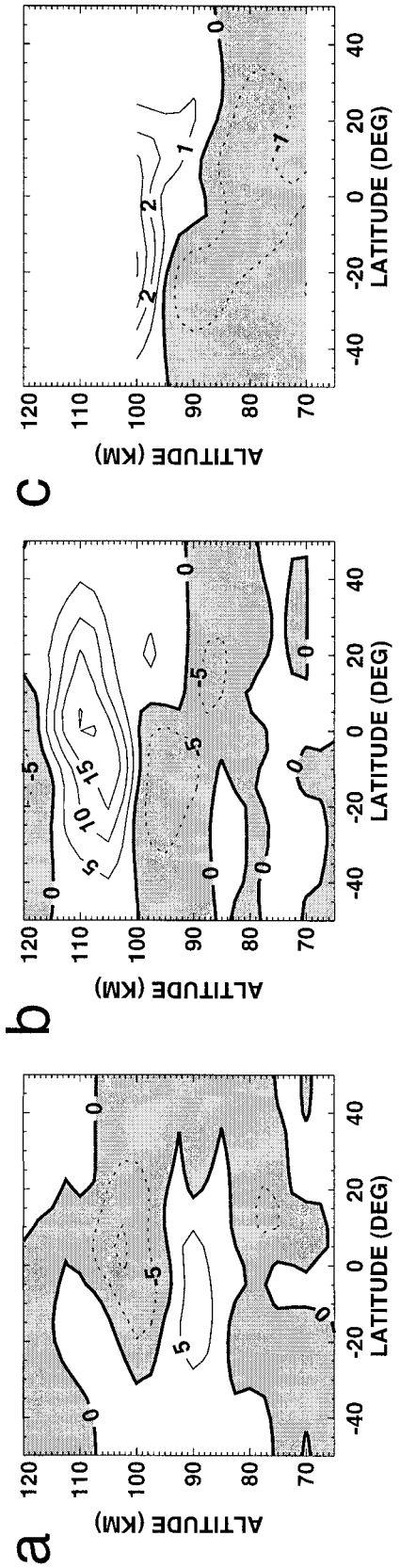

FIG. 12. Eastward $s = 3$ diurnal tide at 0000 UTC and 0° longitude for Aug for (a) meridional wind, (b) zonal wind, and (c) temperature.

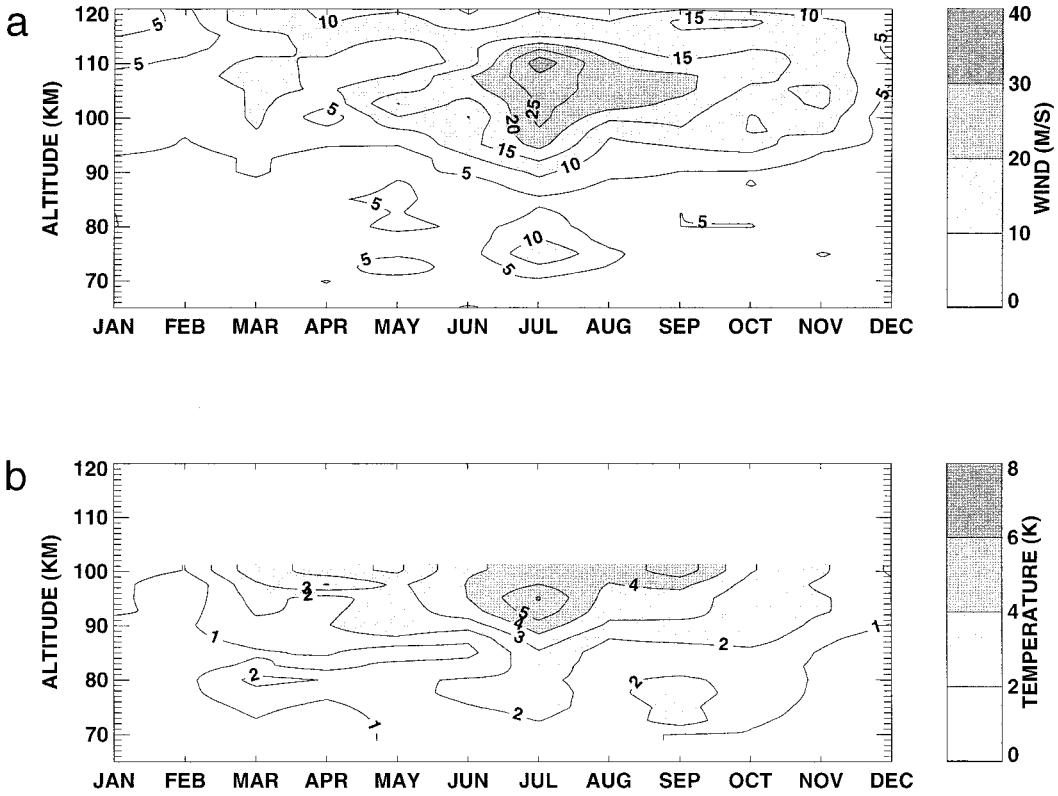

FIG. 13. Amplitude over time and altitude of the eastward diurnal $s = 3$ gravest symmetric mode for (a) zonal wind and (b) temperature.

wind is weakly eastward (Burrage et al. 1996a) and when slow Kelvin waves were not observed (Eckerman and Vincent 1994).

4. Summary and discussion

Asynoptic Fourier analysis of HRDI winds and temperatures reveals features that are consistent with classical predictions of nonmigrating diurnal tides. The zonally symmetric ($s = 0$) tide is the most prominent nonmigrating component, with maximum amplitudes of 6 K in temperature and 30 m s^{-1} in meridional wind. Eastward diurnal tides exhibit similar properties in temperature and in zonal and meridional winds. Classical tidal theory predicts that the temperature amplitude (in Kelvin) would roughly equal that of the winds (in meters per second). The observed meridional wind amplitude is five times that of temperature. The zonal winds generally have slightly lower maximum amplitudes than the meridional wind, and they peak at higher altitudes. The zonal wind is strongest in the $s = 3$ tide, with peak amplitudes of 30 m s^{-1}. The eastward diurnal modes generally showed decreasing phase with height, suggesting upward energy propagation.

The dominant symmetric modes in $s = 0$ meridional wind and temperature, V_2^0 and T_2^0, show increasing phase with altitude. If the phase, ϕ, is interpreted in terms of vertical wavenumber, m, so that $\phi \sim mz$, where z is altitude, then $m > 0$. From linear tidal theory, an eastward frequency and positive vertical wavenumber imply that the averaged vertical energy flux is downward (Wilkes 1949). The HRDI observations interpreted as $s = 0$ diurnal tides, suggest in situ or higher-level forcing. However, it is also possible that this feature corresponds to another alias, namely, a westward diurnal $s = 2$ oscillation (Table 1). The presence of the westward mode is suggested by the phase structure, since a westward frequency and positive vertical wavenumber imply forcing from levels below and therefore consistency with present knowledge of forcing mechanisms.

As mentioned, at 95 km HRDI has well-defined coverage of the horizontal winds at two local times. As a result, it should be possible to separate the contribution of two waves in an observed wave field. However, for $k_{sa} = 1$, such double-node analyses suggest the presence of three separate waves. The presence of a third wave heavily aliases into the spectra of the two waves retrieved. Hence, using data from only two local times is insufficient to accurately decompose the observed wave field into the possible aliases listed in Table 1, and, therefore, we are unable to resolve the question of westward aliasing.

Forcing for both the westward $s = 2$ and the $s = 0$ tides is predicted by the solar excitation of tropospheric

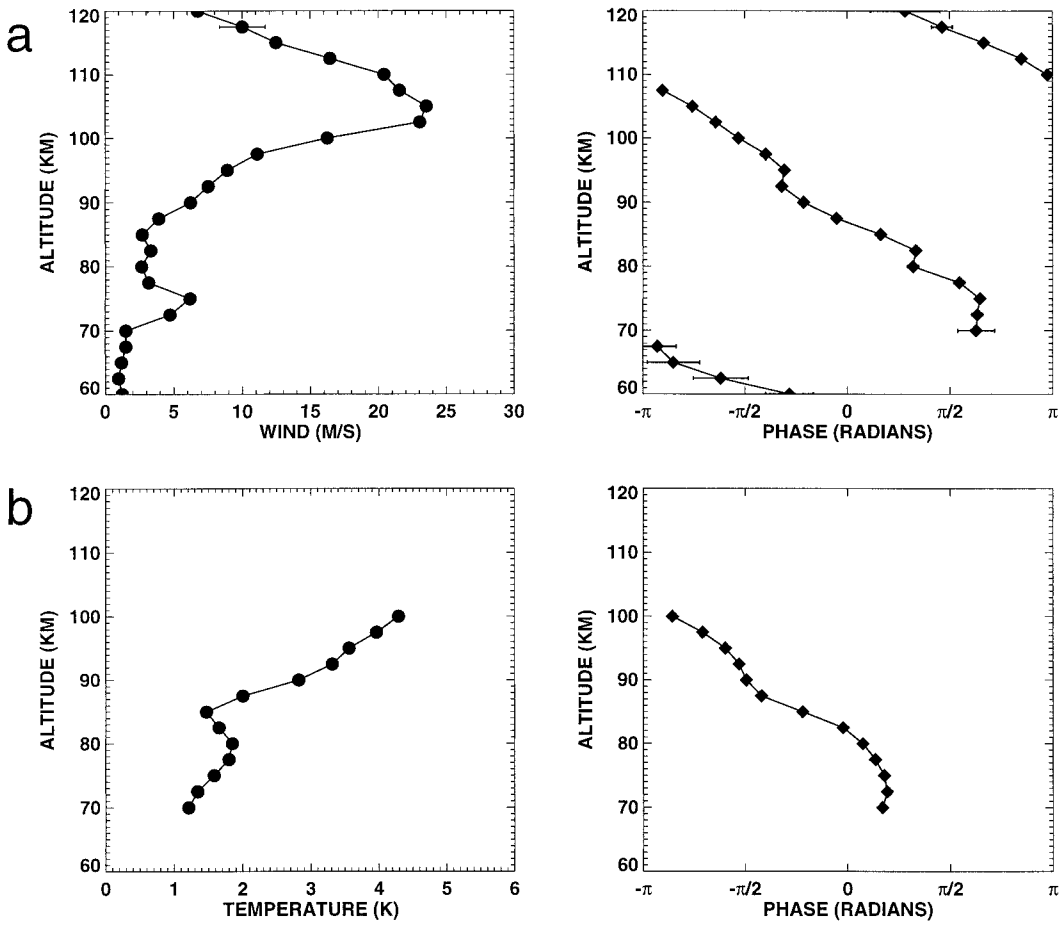

FIG. 14. Vertical structure of the amplitude and phase of the eastward diurnal $s = 3$ gravest symmetric mode for Aug for (a) zonal wind and (b) temperature.

water vapor and the diurnal cycle of latent heat release in the Tropics (Forbes and Groves 1987; Lieberman and Leovy 1995; Williams and Avery 1996). Ekanayake et al. (1997) find that GCM tropospheric forcing produces a weak MLT westward $s = 2$ zonal wind tide (relative to eastward and migrating components) and a negligible $s = 0$ response. The global-scale wave model (GSWM) predicts the $s = 0$ and the westward $s = 2$ diurnal tides (Hagan et al. 1997), as a response to latent heat release. The meridional wind amplitudes of the model $s = 0$ and $s = 2$ responses are comparable to each other, thus bearing out a westward $s = 2$ interpretation of $k_{s_a} = 1$. However, there are major differences between the GSWM tides and HRDI observations. The model tides are a factor of five less than those found in HRDI data. Furthermore, the latitudinal structure of both model tides is inconsistent with the dominant mode found in HRDI data. The question of aliasing in the $s = 0$ field by a westward $s = 2$ tide cannot be resolved as available studies of forcing and theoretical predictions do not provide conclusive support for one interpretation over the other.

The GSWM also predicts some of the Kelvin structure seen in the $s = 3$ zonal wind from forcing due to diurnal deep convective activity. The latitudinal structure of the model zonal wind during October was symmetric and centered at the equator. Moreover, model tidal amplitudes are significant above 95 km. Both these features correspond well to HRDI observations of the gravest symmetric mode in the zonal wind, though the model predicts a slightly lower peak amplitude at a higher altitude. Ekanayake et al. (1997) predict that the eastward $s = 3$ zonal wind is the strongest nonmigrating response in the low-latitude zonal wind.

This study establishes the presence of nonmigrating tides in $s = 0$–3 MLT winds and temperatures. Recent modeling studies of nonmigrating tides agree with some of the features exhibited in HRDI tides. However, questions about the amplitudes and the variable phase behavior observed in the tides still remain. The amount that aliasing contributes to such variability would hopefully be resolved by future satellite observations that sample on three or more nodes. Further study of forcing mechanisms can possibly align model results more with HRDI observations.

Acknowledgments. The authors wish to extend special thanks to Paul Hays for advice, support, and encouragement during this investigation. We also thank the HRDI Science Team, Robert Vincent, Art Richmond, and Jeff Forbes for their constructive comments and valuable suggestions. This study was funded under Contract NAS5-27751 and Grant NAG5-3180.

REFERENCES

Abreu, V. J., A. Bucholtz, P. B. Hays, D. A. Ortland, W. R. Skinner, and J.-H. Yee, 1989: Absorption and emission line shapes in the O_2 atmospheric bands: Theoretical model and limb viewing simulations. *Appl. Opt.,* **28,** 2128–2137.

Burrage, M. D., R. A. Vincent, H. G. Mayr, W. R. Skinner, N. F. Arnold, and P. B. Hays, 1996a: Long term variability in the equatorial middle atmosphere zonal wind. *J. Geophys. Res.,* **101,** 12 847–12 854.

——, and Coauthors, 1996b: Validation of mesospheric and lower thermospheric winds from the High Resolution Doppler Imager. *J. Geophys. Res.,* **101,** 10 365–10 392.

Chapman, S., and R. S. Lindzen, 1970: *Atmospheric Tides.* Gordon and Breach.

Eckerman, S. D., and R. A. Vincent, 1994: First observations of intraseasonal oscillations in the equatorial mesosphere and lower thermosphere. *Geophys. Res. Lett.,* **21,** 265–268.

Ekanayake, E. M. P., T. Aso, and S. Miyahara, 1997: Background wind effect on propagation of nonmigrating diurnal tides in the middle atmosphere. *J. Atmos. Terr. Phys.,* **59,** 401–429.

Forbes, J. M., and G. V. Groves, 1987: Diurnal propagating tides in the low-latitude middle atmosphere. *J. Atmos. Terr. Phys.,* **49,** 153–164.

Hagan, M. E., J. L. Chang, and S. K. Avery, 1997: Global-scale wave model estimates of non-migrating tidal effects. *J. Geophys. Res.,* **102,** 16 349–16 452.

Hamilton, K., 1981: Latent heat release as a possible forcing mechanism for atmospheric tides. *Mon. Wea. Rev.,* **109,** 3–17.

Hays, P. B., V. J. Abreu, M. E. Dobbs, D. A. Gell, H. J. Grassl, and W. R. Skinner, 1993: The High-Resolution Doppler Imager on the Upper Atmosphere Research Satellite. *J. Geophys. Res.,* **98,** 10 713–10 723.

——, D. L. Wu, and The HRDI Science Team, 1994: Observations of the diurnal tide from space. *J. Atmos. Sci.,* **51,** 3077–3093.

Kato, S., 1989: Non-migrating tides. *J. Atmos. Terr. Phys.,* **51,** 673–682.

——, T. Tsuda, and F. Watanabe, 1982: Thermal excitation of nonmigrating tides. *J. Atmos. Terr. Phys.,* **44,** 131–146.

Khattatov, B. V., and Coauthors, 1996: Dynamics of the mesosphere and lower thermosphere as seen by MF radars and by the High Resolution Doppler Imager/UARS. *J. Geophys. Res.,* **101,** 10 393–10 404.

Lieberman, R. S., 1991: Nonmigrating diurnal tides in the equatorial middle atmosphere. *J. Atmos. Sci.,* **48,** 1112–1123.

——, and C. B. Leovy, 1995: A numerical model of nonmigrating diurnal tides between the surface and 65 km. *J. Atmos. Sci.,* **52,** 389–409.

——, and D. Riggin, 1997: High Resolution Doppler Imager observations of Kelvin waves in the equatorial mesophere and lower thermosphere. *J. Geophys. Res.,* **102,** 26 117–26 130.

Lindzen, R. S., 1967: Thermally driven diurnal tide in the atmosphere. *Quart. J. Roy. Meteor. Soc.,* **93,** 18–42.

——, 1978: Effects of daily variations of cumulonimbus activity on the semidiurnal tide. *Mon. Wea. Rev.,* **106,** 526–533.

Morton, Y. T., and Coauthors, 1993: Global mesospheric tidal winds observed by the High Resolution Doppler Imager on board the Upper Atmosphere Research Satellite. *Geophys. Res. Lett.,* **20,** 1263–1266.

Ortland, D. A., P. B. Hays, W. R. Skinner, and J.-H. Yee, 1998: Remote sensing of mesospheric temperature and $O_2(^1\Sigma)$ band volume emission rates with the High Resolution Doppler Imager. *J. Geophys. Res.,* **103,** 1821–1835.

Salby, M. L., 1982: Sampling theory for asynoptic satellite observations. Part I: Space–time spectra, resolution, and aliasing. *J. Atmos. Sci.,* **39,** 2577–2600.

Tsuda, T., and S. Kato, 1989: Diurnal non-migrating tides excited by a differential heating due to land-sea distribution. *J. Meteor. Soc. Japan,* **67,** 43–54.

Wallace, J. M., and R. F. Tadd, 1974: Some further results concerning the vertical structure of atmospheric tidal motions within the lowest 30 kilometers. *Mon. Wea. Rev.,* **102,** 795–803.

Wilkes, M. V., 1949: *Oscillations of the Earth's Atmosphere.* Cambridge University Press.

Williams, C. R., and S. K. Avery, 1996: Diurnal nonmigrating tidal oscillations forced by deep convective clouds. *J. Geophys. Res.,* **101,** 4079–4091.